A Dual Active Bridge DC-DC Converter with Optimal DC-Link Voltage Scaling and Flyback Mode for Enhanced Low-Power Operation in Hybrid PV/Storage Systems

Shahab Poshtkouhi and Olivier Trescases
University of Toronto, 10 King's College Road, Toronto, ON, M5S 3G4, Canada
E-mail: shahab.poshtkouhi@utoronto.ca

***Abstract*—Today's PV micro-inverters (MIVs) provide a modular solution for generation, however the energy storage architectures remain centralized, requiring an additional bi-directional ac-dc converter, with complex cell balancing circuits. Distributing storage capacity within the smart PV panels allows power fluctuations to be locally buffered, while minimizing the need for additional power electronics and balancing circuits. The dual-active-bridge (DAB) topology, which is adopted in this paper, provides bi-directional power flow; however it generally suffers from poor efficiency at low power. It is shown that with a minor modification, the DAB can be operated as a two-transistor flyback converter for improved efficiency. In addition, the dc-link voltage can be dynamically adjusted for the best performance in DAB mode. The proposed control scheme is demonstrated on a 100 W prototype, with up to 8% increase in efficiency at low power.**

***Index Terms*—Photovoltaic (PV) micro-inverters, efficiency, isolated dc-dc stage.**

I. Introduction

The continuous decline of photovoltaic (PV) module prices, compounded with attractive feed-in tariffs in a variety of jurisdictions, is leading to the rapid deployment of PV installations throughout the world [1]. The intermittent nature of PV and other renewable energy resources, and thus the need for energy storage and/or load shedding, is a major challenge in small-scale PV based grids. This is despite the fact that power-quality and other grid strict requirements such as frequency variations are reduced compared to conventional grids. Low-power dc-dc micro-converters (MIC) [2], [3] and ac-dc micro-inverters (MIV) [4], [5] provide high-granularity Maximum Power Point Tracking (MPPT) [6], [7] at the module or sub-string level. This leads to increased robustness to clouds, dirt, and aging effects, as well as irradiance and temperature gradients [7]. A conventional MIV based ac power system is shown in Fig. 1. The Energy Storage System (ESS), which is definitely required for islanded operation on the scale of one or more houses for example, is usually based on a high-power centralized bi-directional ac-dc converter, which is interfaced to a battery bank or a flywheel [8], [9]. Existing MIV architectures satisfy the need for low capital-cost and expandable ac generation, while there is compelling argument to extend this technology to include small-scale distributed storage. A novel topology with distributed storage is proposed

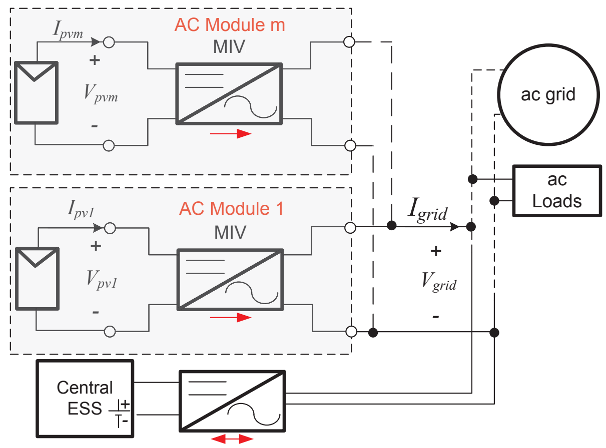

Fig. 1. Conventional micro-inverter based PV system with central ESS.

in [10] for grid stabilization, while saving fuel, and improving the generator lifetime. MIV Integrated storage helps to buffer the frequent irradiance fluctuations, while also providing local back-up power and reactive power support [11], [12]. A low-power single-stage multi-port converter for PV and battery is proposed in [13], while a 3-kW interconnection of a battery pack and a PV module through an isolated dc-dc converter is discussed in [14]. The general architecture of a two-stage MIV with an integrated ESS is shown in Fig. 2. While two-stage MIVs have a slightly lower efficiency than single-stage MIVs, the high-voltage dc link capacitance, C_{bus}, can be used for ac power decoupling in single-phase systems [15], [16].

Interfacing the low-voltage dc storage, either batteries or ultra-capacitors, directly to the PV bus is preferable for high efficiency [14]. Lithium-ion ultra-capacitors [17], which offer 2-4× higher specific energy than conventional Electric Double Layer Capacitors and can withstand more than 200000 charge/discharge cycles, are an attractive future candidate for short-term MIV integrated storage. The focus of this work is on the front-end dc-dc stage.

The objective of this paper is to 1) discuss a bi-directional isolated dc-dc stage for the PV-bus connection, which is already presented in [10] and 2) demonstrate a novel low-power operating mode and dynamic dc-link optimization scheme to maintain high efficiency over a broad power range. This is crucial in any commercial MIV architecture; for example the European Efficiency index dedicates 32% of the total evaluation weight to operation below 30% of the rated power [18].

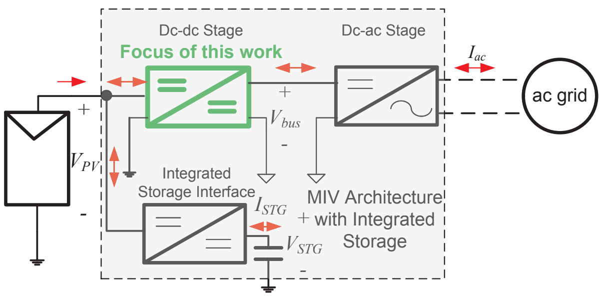

Fig. 2. Two-stage MIV architecture with integrated storage [10].

II. Proposed DAB Architecture and Principle of Operation

The proposed dc-dc architecture is shown in Fig. 3(a). This converter is a modified Dual-Active-Bridge (DAB) that interfaces V_{pv} with the dc link, V_{bus}.

A. DAB Mode

The DAB topology was selected based on (1) galvanic isolation, (2) soft-switching operation and (3) simple phase-shift power control [19], [20]. In addition, the DAB topology is bi-directional, therefore the storage can be used to transfer energy to/from other elements in the grid. The average power from V_{pv} to V_{bus}, P, is

$$P = \frac{V_{PV} V_{bus}}{n \omega_s L_{DAB}} \phi (1 - \frac{\phi}{\pi}), \quad (1)$$

where n is the transformer's turns ratio, L_{DAB} is the DAB inductance, which is the sum of transformer's leakage inductance, L_{leak}, and an optional external inductance, L_{ext}. ϕ is the phase-shift between the two bridges, and $\omega_s = 2\pi f_s$, where f_s is the switching frequency.

The switching waveforms of the DAB converter are shown in Fig. 4(a). The slopes of the DAB inductance current, I_{LDAB}, in switching states I and II are respectively calculated as

$$s_1 = \frac{V_{PV} + \frac{V_{bus}}{n}}{L_{DAB}}, \quad (2)$$

$$s_2 = \frac{-V_{PV} + \frac{V_{bus}}{n}}{L_{DAB}}. \quad (3)$$

In two-stage MIV architectures, V_{bus} is generally regulated to a fixed voltage by the inverter stage. The reference voltage, V^*_{bus}, is usually chosen to optimize efficiency at the nominal operating point [7]. It can be shown that the DAB converter achieves turn-on Zero-Voltage-Switching (ZVS) and maximum efficiency when $V_{bus} = nV_{PV}$, as the reactive circulating current is minimized [19].

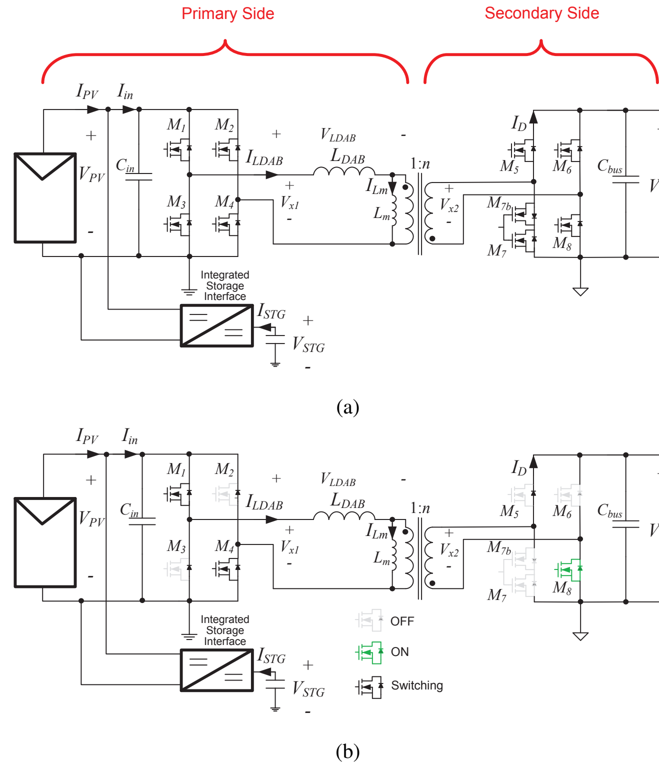

Fig. 3. a) Proposed modified DAB dc-dc architecture for improved low power efficiency. b) Switch configuration in Flyback mode.

In order to minimize the losses in the DAB, the reference DC link voltage, V^*_{bus}, is dynamically adjusted in the inverter stage such that $V^*_{bus} = nV_{MPP}$, where V_{MPP} is the PV MPP voltage. It is well-known that V_{MPP} undergoes a relatively low fluctuation of about 30% during the course of a typical day [21]. This is in contrast to the PV current at MPP, I_{MPP}, which is proportional to irradiance and thus has large-scale fluctuations, especially on cloudy days.

B. Flyback Mode

A typical PV generation system spends more than two-thirds of the time operating below 50% of its rated power [7]. The conventional DAB converter suffers from relatively poor efficiency at low power due to high switching and drive losses [19], hence the need for a dedicated low-power mode. By driving M_1 and M_4 simultaneously on the primary side, the converter can be operated as a two-transistor flyback converter (2T-flyback) [22]. The switch configuration in Flyback mode is shown in Fig. 3(b). The switches M_1 and M_4 remain active, M_8 is kept *on* and all other switches are *off*. The secondary-side bridge is slightly modified with the addition of one switch, M_{7b}, to achieve bi-directional blocking capability in Flyback mode. The charging and discharging slopes of the magnetizing

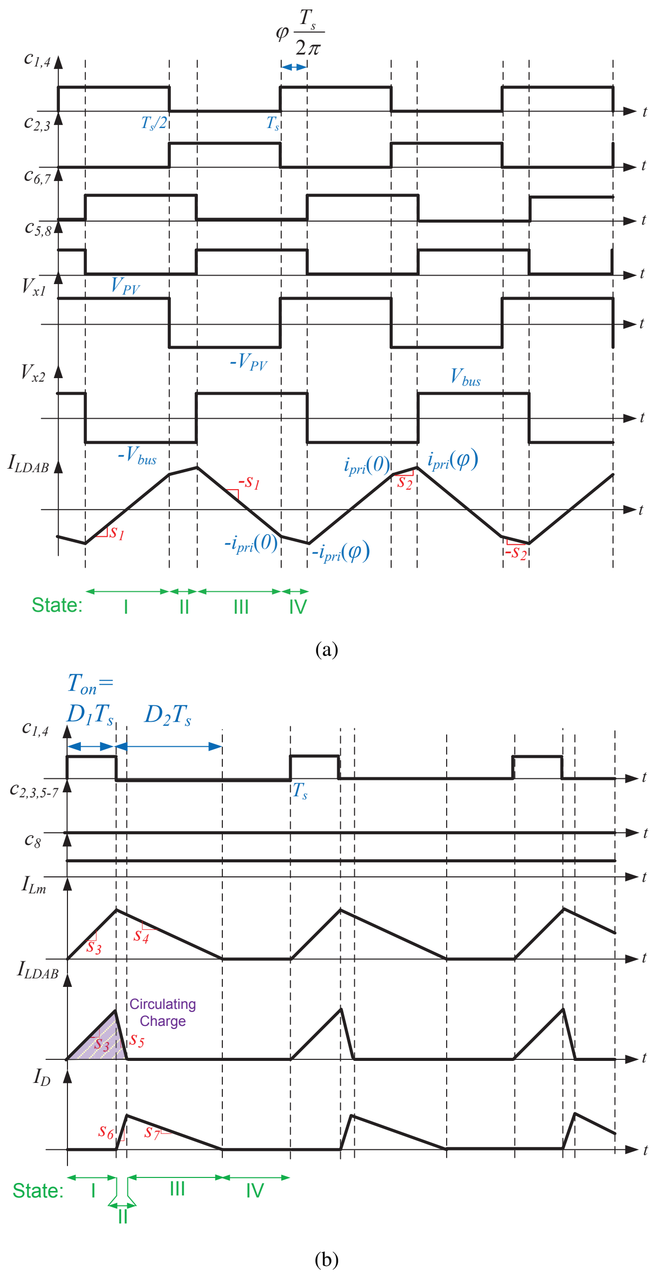

Fig. 4. Switching waveforms in (a) DAB mode, and (b) Flyback mode.

inductance current, I_{L_m}, are given by

$$s_3 = \frac{V_{PV}}{L_{DAB} + L_m}, \tag{4}$$

$$s_4 = \frac{-V_{bus}}{nL_m}. \tag{5}$$

The DAB inductance circulates charge in every switching period in this mode. The charging slope of I_{LDAB} is the same as s_3 and the discharging slope is

$$s_5 = \frac{-V_{PV} - \frac{V_{bus}}{n}}{L_{DAB}}. \tag{6}$$

Finally, the output diode's current, I_D, delivers charge to the bus with the following slopes in switching states II and III

$$s_6 = \frac{s_4 + s_5}{n}, \tag{7}$$

$$s_7 = \frac{s_4}{n}. \tag{8}$$

The 2T-flyback topology exhibits several advantages over DAB mode for low power conditions, including less switching and gate-drive losses (two switching devices versus nine in the DAB mode). Unlike the more conventional single transistor flyback topology, the body diodes of M_2 and M_3 clamp the drain voltage on the switching devices M_1 and M_4, which reduces Electromagnetic Interference (EMI) and limits the blocking voltage rating on the primary switches to V_{PV}. The Flyback mode is operated with fixed on-time, T_{on}, in Pulse Frequency Modulation (PFM) mode [23], where T_{on} is given by

$$T_{on} = D_1 T_s, \tag{9}$$

where D_1 is the duty cycle in Flyback mode, and T_s is the switching period.

The corresponding waveforms of the converter are shown in Fig. 4(b). There are two inherent limitations to the 2T-flyback topology: 1) D_1 must be less than 50% in order to avoid transformer saturation, and 2) V_{bus} must be less than nV_{pv}, to ensure that the body diode of M_5 transfers power to V_{bus} when the primary-side switches are *off*. As a result, V_{bus} needs to be reduced in Flyback mode. The presence of L_{DAB} results in additional losses, since it circulates current in a switching period. The energy captured in L_{DAB} is transferred back to the input capacitance, C_{in}, in the 2T-flyback topology, as opposed to a conventional flyback scheme, which does not provide a return path for the charge in the leakage inductance. In addition, L_{DAB} results in the soft turn-on of the output diode.

The Flyback mode exhibits uni-directional power transfer. The converter can operate with reverse power flow by adding another switch on the primary side. This additional switch is not included in the experimental prototype, as the efficiency in DAB mode is sensitive to conduction losses at the low-voltage, high-current primary-side. While possible, reverse power capability is not strictly needed in low-power Flyback mode; the DAB can be prevented from operating in this condition by adopting burst-mode control instead, albeit at slightly lower efficiency than Flyback mode.

C. Dual Mode Control

The conceptual control diagram of the converter is shown in Fig. 5. c_{1-8} denote the gating voltages for switches M_{1-8}. The DAB mode is adopted if P is higher than a threshold value, P_{thresh}, or if P is negative, in which case the storage is charged directly from the bus. In DAB mode, ϕ is controlled to regulate the power flow to/from the dc-ac stage, while the storage element's State-of-Charge (SOC) and MPPT operation can be controlled by the dedicated interface converter.

In Flyback mode, T_s is adjusted by the controller, $G_{c2}(s)$, in order to regulate P to P^*. Assuming that the magnetizing inductance of the transformer, L_m, is much larger than L_{DAB}, the power flow is given by

$$P = \frac{(V_{PV} D_1)^2 T_s}{2L_m}. \tag{10}$$

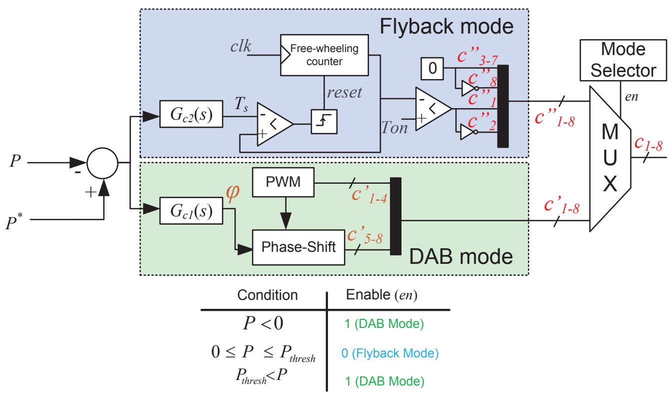

Fig. 5. Simplified conceptual control diagram.

III. Efficiency Analysis

This section discusses the dominant power losses in the DAB and Flyback modes.

A. Conduction Losses

As shown in Fig. 4(a), the current into the leakage inductor and primary winding of the transformer approach a perfect trapezoid when $V_{bus} = nV_{pv}$. The following equation for the RMS current at the primary side of transformer, I_{pri}, can be obtained [24]

$$I_{pri} = \frac{1}{3\pi}(i_{pri}(0)^2\gamma + i_{pri}(\phi)^2(\phi - \gamma) + (\pi - \phi)(i_{pri}(0)^2 + i_{pri}(\phi)^2 - i_{pri}(0)i_{pri}(\phi)), \tag{11}$$

where

$$\gamma = \frac{i_{pri}(0)}{i_{pri}(0) - i_{pri}(\phi)}, \tag{12}$$

and $i_{pri}(0)$ and $i_{pri}(\phi)$ are the instantaneous currents of the transformer at the primary side at times $t = 0$ and $t = \frac{\phi}{\omega_s}$, respectively. These can be easily calculated considering the symmetry of the transformer current [24]

$$i_{pri}(0) = \frac{1}{2L_{DAB}\omega_s}(\pi V_{PV} - (\pi - 2\phi)V_{bus}), \tag{13}$$

$$i_{pri}(\phi) = \frac{1}{2L_{DAB}\omega_s}((\pi - 2\phi)V_{PV} - \pi V_{bus}). \tag{14}$$

Similar calculations can be done for the transformer's secondary side RMS current, I_{sec}. Two primary and two secondary switches are conducting at each instance in DAB mode. Thus, the conduction losses in this mode are approximated by

$$P_{DAB,cond} = (2R_{on,pri} + R_{L_{DAB}})I_{pri}^2 + 2.5R_{on,sec}I_{sec}^2, \tag{15}$$

where $R_{on,pri}$ and $R_{on,sec}$ are the primary and secondary side switches' on-resistances respectively, and $R_{L_{DAB}}$ is the lumped winding resistance of the transformer and inductor. The factor of 2.5× on the secondary side comes from the fact that, there are two back-to-back switches, M_7, and M_{7b} on one leg in the secondary side to support the flyback operation.

Neglecting the clamping diodes' conduction interval, the RMS current for the two switches, I_{M_1,M_4}, and in the output diode, D, in the 2T-flyback converter can be obtained as [25]

$$I_{M_1,M_4} = \frac{nP\sqrt{D_1}}{V_{bus}(1 - D_1)}, \tag{16}$$

$$I_D = \frac{D_2 T_s V_{bus}}{n^2 L_m}\sqrt{\frac{D_2}{3}}, \tag{17}$$

where D_2 is approximated by the following

$$D_2 = \frac{nV_{PV}D_1}{V_{bus}}. \tag{18}$$

The total conduction loss in Flyback mode is

$$P_{Flbk,cond} = (2R_{on,pri} + R_{L_{DAB}})I_{M1}^2 + V_F I_D + R_{on,sec}I_D^2, \tag{19}$$

where V_F is the output diode's forward voltage.

B. Switching Losses

The switches in DAB mode can be turned *on* realizing Zero Voltage Switching (ZVS) [24]. However the turn-*off* losses are not eliminated. The total switching losses in this mode can be approximated by

$$P_{DAB,sw} = \frac{1}{2}f_s t_{off}(V_{pv}(i_{pri}(0) + i_{pri}(\phi) + V_{bus}(i_{sec}(0) + i_{sec}(\phi)), \tag{20}$$

where t_{off} is the turn-*off* time of the MOSFETs.

Switches M_1 and M_2 exhibit hard switching at turn-*off* in Flyback mode. Thus, the corresponding switching loss in Flyback mode can be approximated as

$$P_{Flbk,sw} = \frac{V_{PV}^2 D_1 t_{off}}{2(L_{DAB} + L_m)}. \tag{21}$$

The switch drive losses are not considered here; However, there are nine switches actively driven in DAB mode compared to only two switches actively switching in Flyback mode. Furthermore, f_s is much lower in Flyback mode then in DAB mode, which further reduces the switch drive losses.

C. Core Losses

Core losses are present in the high-frequency transformer in both DAB and Flyback modes and can be approximated using the Steinmetz equation [26]

$$P_{core} = k f_s^{\alpha} B_{peak}^{\beta}, \tag{22}$$

where B_{peak} is the peak flux density, and k, α, and β are the Steinmetz parameters, which depend on the core, and are usually found by curve fitting. Core losses constitute a low percentage of the total losses in DAB mode [24] due to high-frequency ac-ac operation. However, core losses are dominant in Flyback mode. This is due to high peaks in core voltage, and lower frequency operation, which increases B_{peak} in the transformer.

This analysis neglects the skin effect in all conductors, which can be significant, especially in DAB mode due to high frequency operation.

D. Loss Comparison in Two Modes

The calculated loss breakdown for P = 10 W and P = 40 W is shown in Fig. 6. The conduction losses in all active and passive elements are lumped together. The switching losses also include the drive losses. In Flyback mode, the switching losses are reduced by at least 10×, mostly by eliminating the turn-*off* losses on the high voltage side, at a cost of marginally increase in conduction losses. The transformer and inductor core loss is slightly higher in Flyback mode, due to higher B_{peak}. The core losses in Flyback mode increase rapidly with the power due to higher B_{peak} and f_s. This is not the case for the DAB converter, in which the core losses remain almost constant over the power range.

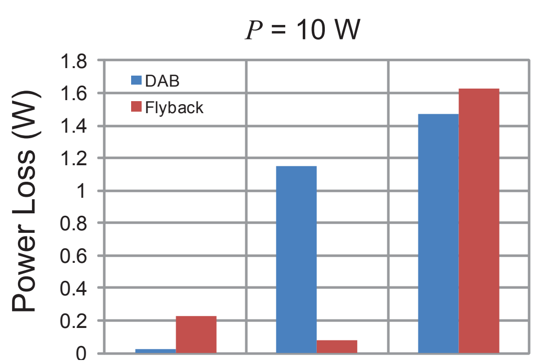

(a)

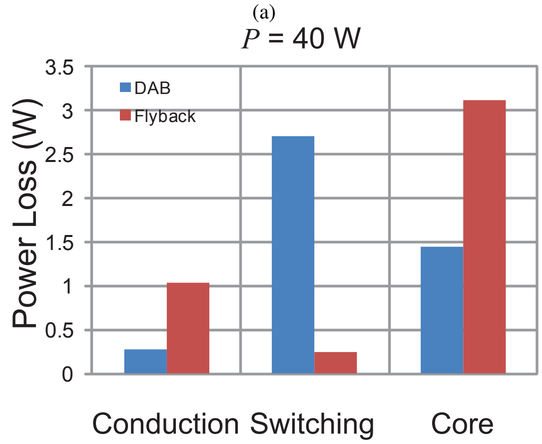

(b)

Fig. 6. Simulated power losses for (a) P = 10 W, and (b) P = 40 W.

IV. Experimental Results

A prototype of the system shown in Fig. 3(a) was fabricated on a custom Printed Circuit Board, with DAB power rating of 100 W. The specifications of the prototype are listed in Table I. The converters are digitally controlled using an on-

TABLE I
MIV Prototype Specifications

Parameter	Value	Units
Rated Power, P_{nom}	100	W
Dc-dc Stage Switching Frequency, f_s		
DAB Mode	195	kHz
Flyback Mode	20-50	kHz
Fixed On-Time, T_{on}	8	μs
Input Capacitance, C_{in}	300	μF
Bus Capacitance, C_{bus}	100	μF
DAB Inductance, L_{DAB}	4.2	μH
Magnetizing Inductance, L_m	32	μH
Bus Voltage Range, V_{bus}		
DAB mode	200-270	V
Flyback mode	170	V
Transformer Turns Ratio, n	9	

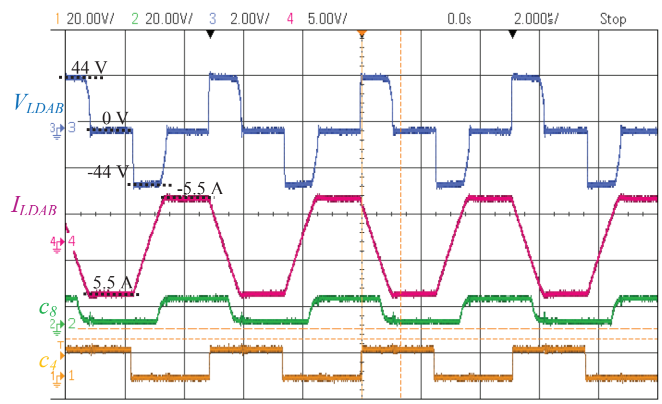

(a)

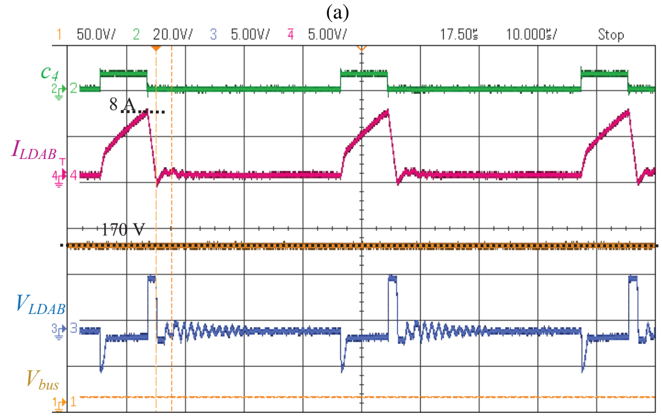

(b)

Fig. 7. Steady-state waveforms of the converter in (a) DAB mode at V_{PV} = 22 V (I_{LDAB}:5 A/div), and (b) Flyback mode at V_{PV} = 25 V (I_{LDAB}:5 A/div).

board FPGA. A custom planar transformer was designed to reduce the weight and profile of the prototype. The steady-state waveforms in DAB and Flyback modes at P = 70 W, and P = 15 W, are shown in Fig. 7(a) and (b), respectively. V_{bus} is adjusted to nV_{PV} in DAB mode to achieve optimal efficiency, as it is illustrated by the flat portions in I_{LDAB}. The closed-loop dynamic response of Flyback mode for a step

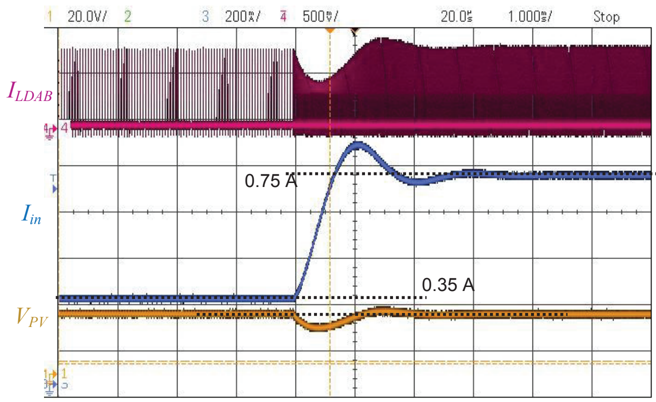

Fig. 8. Step response of Flyback mode with the integrated storage interface off: P: 9.1 W $\rightarrow$ 19.5 W (I_{in}:0.2 A/div, I_{LDAB}: 10 A/div).

change in P^*, while the dedicated integrated storage converter is off, is shown in Fig. 8. f_s is increased in Flyback mode by the controller to accommodate the higher input power.

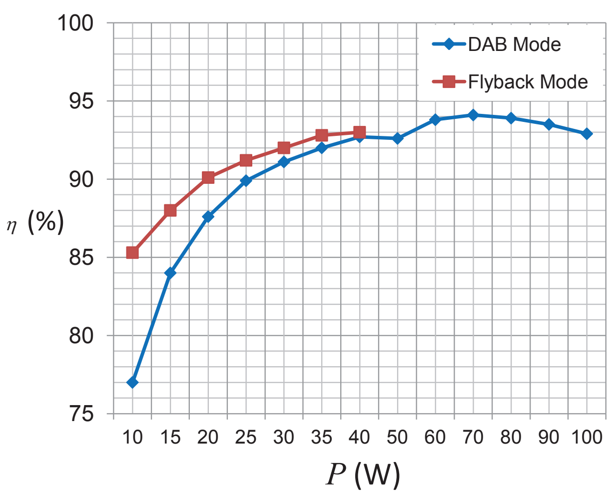

Fig. 9. Measured efficiency, η, of the converter.

The measured efficiency of the converter, η, in both modes is shown in Fig. 9. A peak efficiency of 94% is achieved in DAB mode, while Flyback mode has a superior efficiency up to P = 40 W. The power is limited in Flyback mode due to the maximum duty ratio of 50%. However, the design is such that the two efficiency curves intercept at a point close to the maximum transferrable power in Flyback mode. The converter operates at the edge of Discontinuous Conduction Mode (DCM) at the intercept point, such that the operation is switched to DAB mode at higher power.

V. Conclusions

A novel DAB switching scheme was introduced for the dc-dc stage of module integrated power converters for PV applications. The modified flyback switching scheme exhibits 8% higher efficiency than DAB mode at 10 W, which comes at the cost of an additional switch. While Flyback mode exhibits more core losses and slightly more conduction losses compared to DAB mode, the switching losses are significantly reduced by eliminating most of the switching actions, and reducing the frequency.

Acknowledgement

This work was supported by Solantro Semiconductor, the Ontario Centres of Excellence, the Natural Sciences and Engineering Research Council of Canada, the Canadian Foundation for Innovation and the Ontario Research Fund. The authors also thank Ray Orr, Ben Bacque, Mihai Varlan, and Chris Gerolami for discussions related to nanogrids and micro-inverters.

References

[1] P. Denholm, R. Margolis, T. Mai, G. Brinkman, E. Drury, M. Hand, and M. Mowers, "Bright future: Solar power as a major contributor to the u.s. grid," *IEEE Power and Energy Magazine*, vol. 11, no. 2, pp. 22–32, 2013.

[2] R. K. Hester, C. Thornton, S. Dhople, Z. Zhao, N. Sridhar, and D. Freeman, "High efficiency wide load range buck/boost/bridge photovoltaic microconverter," in *IEEE Applied Power Electronics Conference and Exposition*, 2011, pp. 309 –313.

[3] B. York, W. Yu, and J.-S. Lai, "An integrated boost resonant converter for photovoltaic applications," *IEEE Transactions on Power Electronics*, vol. 28, no. 3, pp. 1199–1207, 2013.

[4] R. Erickson and A. Rogers, "A microinverter for building-integrated photovoltaics," in *IEEE Applied Power Electronics Conference and Exposition*, 2009, pp. 911 –917.

[5] "Enphase m190 microninveter," Enphase Datasheet, 2009, available http://enphaseenergy.com.

[6] N. Femia, G. Lisi, G. Petrone, G. Spagnuolo, and M. Vitelli, "Distributed maximum power point tracking of photovoltaic arrays: Novel approach and system analysis," *IEEE Transactions on Industrial Electronics*, vol. 55, no. 7, pp. 2610 –2621, July 2008.

[7] S. Poshtkouhi, V. Palaniappan, M. Fard, and O. Trescases, "A general approach for quantifying the benefit of distributed power electronics for fine grained mppt in photovoltaic applications using 3-d modeling," *IEEE Transactions on Power Electronics*, vol. 27, no. 11, pp. 4656–4666, 2012.

[8] L. Xu and D. Chen, "Control and operation of a dc microgrid with variable generation and energy storage," *IEEE Transactions on Power Delivery*, vol. 26, no. 4, pp. 2513–2522, 2011.

[9] G. Suvire, M. Molina, and P. Mercado, "Improving the integration of wind power generation into ac microgrids using flywheel energy storage," *IEEE Transactions on Smart Grid*, vol. 3, no. 4, pp. 1945–1954, 2012.

[10] S. Poshtkouhi, M. Fard, H. Hussein, L. Dos Santos, O. Trescases, M. Varlan, and T. Lipan, "A Dual-Active-Bridge based Bi-Directional Micro-Inverter with Integrated Short-Term Li-Ion Ultra-Capacitor Storage and Active Power Smoothing for Modular PV Systems," in press.

[11] M. Alam, K. Muttaqi, and D. Sutanto, "Mitigation of rooftop solar pv impacts and evening peak support by managing available capacity of distributed energy storage systems," *IEEE Transactions on Power Systems*, vol. PP, no. 99, pp. 1–11, 2013.

[12] L. Liu, H. Li, Z. Wu, and Y. Zhou, "A cascaded photovoltaic system integrating segmented energy storages with self-regulating power allocation control and wide range reactive power compensation," *IEEE Transactions on Power Electronics*, vol. 26, no. 12, pp. 3545–3559, 2011.

[13] Y.-M. Chen, A. Huang, and X. Yu, "A high step-up three-port dc-dc converter for stand-alone pv/battery power systems," *IEEE Transactions on Power Electronics*, vol. 28, no. 11, pp. 5049–5062, 2013.

[14] Z. Wang and H. Li, "An integrated three-port bidirectional dc-dc converter for pv application on a dc distribution system," *IEEE Transactions on Power Electronics*, vol. 28, no. 10, pp. 4612–4624, 2013.

[15] H. Hu, S. Harb, N. Kutkut, Z. Shen, and I. Batarseh, "A single-stage microinverter without using eletrolytic capacitors," *IEEE Transactions on Power Electronics*, vol. 28, no. 6, pp. 2677–2687, June 2013.

[16] S. Kjaer, J. Pedersen, and F. Blaabjerg, "A review of single-phase grid-connected inverters for photovoltaic modules," *IEEE Transactions on Industry Applications*, vol. 41, no. 5, pp. 1292–1306, Sept 2005.

[17] "Lithium-Ion Capacitor," JSR Micro, 2012, available at http://www.jsrmicro.com/index.php/EnergyAndEnvironment/.

[18] "European or CEC Efficiency," available at http://files.pvsyst.com/help/index.html.

[19] F. Krismer and J. Kolar, "Efficiency-optimized high-current dual active bridge converter for automotive applications," *IEEE Transactions on Industrial Electronics*, vol. 59, no. 7, pp. 2745–2760, 2012.

[20] H. Qin and J. Kimball, "Generalized average modeling of dual active bridge dc-dc converter," *IEEE Transactions on Power Electronics*, vol. 27, no. 4, pp. 2078–2084, 2012.

[21] M. Park and I.-K. Yu, "A study on the optimal voltage for mppt obtained by surface temperature of solar cell," in *30th Annual Conference of IEEE Industrial Electronics Society, 2004*, vol. 3, 2004, pp. 2040–2045 Vol. 3.

[22] D. D. C. Lu, H.-C. Iu, and V. Pjevalica, "A single-stage ac/dc converter with high power factor, regulated bus voltage, and output voltage," *IEEE Transactions on Power Electronics*, vol. 23, no. 1, pp. 218–228, 2008.

[23] R. Erickson and D. Maksimović, *Fundamentals of Power Electronics, Second Ed.* Springer, 2001.

[24] H. Qin and J. Kimball, "Generalized average modeling of dual active bridge dc-dc converter," *IEEE Transactions on Power Electronics*, vol. 27, no. 4, pp. 2078–2084, April 2012.

[25] D. Murthy-Bellur and M. Kazimierczuk, "Two-switch flyback-forward pwm dc-dc converter with reduced switch voltage stress," in *Proceedings of 2010 IEEE International Symposium on Circuits and Systems (ISCAS)*, May 2010, pp. 3705–3708.

[26] J. Reinert, A. Brockmeyer, and R. De Doncker, "Calculation of losses in ferro- and ferrimagnetic materials based on the modified steinmetz equation," *IEEE Transactions on Industry Applications*, vol. 37, no. 4, pp. 1055–1061, Jul 2001.